

## **Atmospheric Characterization During Super-Resolution Vision System Developmental Testing**

**by M. Sean D'Arcy, David Tofsted, Edward Creegan, and Robert Brice**

**ARL-TR-6454**

**May 2013**

## **NOTICES**

### **Disclaimers**

The findings in this report are not to be construed as an official Department of the Army position unless so designated by other authorized documents.

Citation of manufacturer's or trade names does not constitute an official endorsement or approval of the use thereof.

Destroy this report when it is no longer needed. Do not return it to the originator.

# **Army Research Laboratory**

White Sands Missile Range, NM 88002-5501

---

**ARL-TR-6454****May 2013**

---

## **Atmospheric Characterization During Super-Resolution Vision System Developmental Testing**

**M. Sean D'Arcy, David Tofsted, Edward Creegan, and Robert Brice**  
**Computational and Information Sciences Directorate, ARL**

REPORT DOCUMENTATION PAGE				Form Approved OMB No. 0704-0188	
Public reporting burden for this collection of information is estimated to average 1 hour per response, including the time for reviewing instructions, searching existing data sources, gathering and maintaining the data needed, and completing and reviewing the collection information. Send comments regarding this burden estimate or any other aspect of this collection of information, including suggestions for reducing the burden, to Department of Defense, Washington Headquarters Services, Directorate for Information Operations and Reports (0704-0188), 1215 Jefferson Davis Highway, Suite 1204, Arlington, VA 22202-4302. Respondents should be aware that notwithstanding any other provision of law, no person shall be subject to any penalty for failing to comply with a collection of information if it does not display a currently valid OMB control number. <b>PLEASE DO NOT RETURN YOUR FORM TO THE ABOVE ADDRESS.</b>					
1. REPORT DATE (DD-MM-YYYY) May 2013		2. REPORT TYPE Final		3. DATES COVERED (From - To) November 12–15, 2012	
4. TITLE AND SUBTITLE Atmospheric Characterization During Super-Resolution Vision System Developmental Testing				5a. CONTRACT NUMBER	
				5b. GRANT NUMBER	
				5c. PROGRAM ELEMENT NUMBER	
6. AUTHOR(S) M. Sean D'Arcy, David Tofsted, Edward Creegan, and Robert Brice				5d. PROJECT NUMBER	
				5e. TASK NUMBER	
				5f. WORK UNIT NUMBER	
7. PERFORMING ORGANIZATION NAME(S) AND ADDRESS(ES) U.S. Army Research Laboratory ATTN: RDRL-CIE-D White Sands Missile Range, NM 88002-5501				8. PERFORMING ORGANIZATION REPORT NUMBER ARL-TR-6454	
9. SPONSORING/MONITORING AGENCY NAME(S) AND ADDRESS(ES)				10. SPONSOR/MONITOR'S ACRONYM(S)	
				11. SPONSOR/MONITOR'S REPORT NUMBER(S)	
12. DISTRIBUTION/AVAILABILITY STATEMENT  Approved for public release; distribution is unlimited.					
13. SUPPLEMENTARY NOTES michael.s.darcy.civ@mail.mil					
14. ABSTRACT The Super-Resolution Vision System is a DARPA-sponsored project designed to create an imaging system that can “see” more sharply through optical turbulence. The system has integrated several image processing techniques into a modular package. To test the system, measurements of optical targets at ranges up to 2 km were collected at White Sands Missile Range, NM, between 13 and 15 November, 2012. This report documents the atmospheric characterization performed in support of that test to measure winds and turbulence strength present. Weather conditions during much of the test period were dry and clear, except during the afternoon of November 15. Turbulence strength ( $C_n^2$ ) reached $2 \times 10^{-13} \text{ m}^{-2/3}$ during much of the daylight hours (0900 to 1500), providing a stressing environment for much of the testing period. Meteorological data were collected from 0630 through 1630 local time each day of the test. RM Young 81000 sonic anemometers were located at 0-, 800-, and 1800-m target points at 1.5-m elevation to provide point estimates of $C_n^2$ . Sonic anemometer data were also collected at a 0-km tower at several levels, providing a vertical turbulence profile. Turbulence data were also collected optically using scintillometers over 800- and 1800-m paths.					
15. SUBJECT TERMS atmospheric optics, atmospheric turbulence					
16. SECURITY CLASSIFICATION OF:			17. LIMITATION OF ABSTRACT  UU	18. NUMBER OF PAGES  50	19a. NAME OF RESPONSIBLE PERSON M. Sean D'Arcy
a. REPORT Unclassified	b. ABSTRACT Unclassified	c. THIS PAGE Unclassified			19b. TELEPHONE NUMBER (Include area code) 575-678-1997



---

## Contents

---

<b>List of Figures</b>	<b>iv</b>
<b>List of Tables</b>	<b>vii</b>
<b>1. Introduction</b>	<b>1</b>
<b>2. Weather During the Test</b>	<b>7</b>
<b>3. Atmospheric Instrumentation and Analysis</b>	<b>8</b>
<b>4. Estimation of <math>C_n^2</math> from Sonic Anemometer Data</b>	<b>11</b>
<b>5. Data Plots</b>	<b>14</b>
<b>6. Derived Results</b>	<b>32</b>
<b>7. Conclusions</b>	<b>36</b>
<b>8. References</b>	<b>37</b>
<b>List of Symbols, Abbreviations, and Acronyms</b>	<b>38</b>
<b>Distribution List</b>	<b>39</b>

---

## List of Figures

---

Figure 1. Typical vegetation and earthen berms in distance at EOVAF range. ....	2
Figure 2. EOVAF range site map for targets, observation points, and sonic anemometer measurement points.....	3
Figure 3. Six-spoke radial bar target image. ....	5
Figure 4. Pseudo-fractal (multi-resolution) target image. ....	6
Figure 5. Various replica military weapon targets viewed. ....	6
Figure 6. Common objects used as false alarm targets.....	7
Figure 7. Downrange tripod with mounted 81000 RM Young sonic anemometer.....	9
Figure 8. Meteorological tower with sonic anemometers at 2, 4, 6, and 8 m. ....	10
Figure 9. Lockheed scintillometer transmitter shown just above horizon formed by 800-m berm. ....	11
Figure 10. The 800-m Lockheed Scintillometer Data collected on 13 November. ....	15
Figure 11. The 1800-m Scintec BLS 450 Scintillometer Data collected on 13 November. ....	16
Figure 12. The 800-m Lockheed Scintillometer Data collected on 14 November. ....	16
Figure 13. The 1800-m Scintec BLS 450 Scintillometer Data collected on 14 November. ....	17
Figure 14. The 800-m Lockheed Scintillometer Data collected on 15 November. ....	17
Figure 15. The 1800-m Scintec BLS 450 Scintillometer Data collected on 15 November. ....	18
Figure 16. DUT building area sonic estimated turbulence strength for 13 November. ....	19
Figure 17. The 800-m target area sonic estimated turbulence strength for 13 November. ....	20
Figure 18. The 1800-m target area sonic estimated turbulence strength for 13 November. ....	20

Figure 19. Tower sonic estimated $C_n^2$ Data from 2-m level, 13 November. ....	21
Figure 20. Tower sonic estimated $C_n^2$ Data from 4-m level, 13 November. ....	21
Figure 21. Tower sonic estimated $C_n^2$ Data from 6-m level, 13 November. ....	22
Figure 22. Tower sonic estimated $C_n^2$ Data from 8-m level, 13 November. ....	22
Figure 23. DUT building area sonic estimated turbulence strength for 14 November. ....	24
Figure 24. The 800-m target area sonic estimated turbulence strength for 14 November. ....	24
Figure 25. The 1800-m target area sonic estimated turbulence strength for 14 November. ....	25
Figure 26. Tower sonic estimated $C_n^2$ data from 2-m level, 14 November. ....	25
Figure 27. Tower sonic estimated $C_n^2$ Data from 4-m level, 14 November. ....	26
Figure 28. Tower sonic estimated $C_n^2$ Data from 6-m level, 14 November. ....	26
Figure 29. Tower sonic estimated $C_n^2$ Data from 8-m level, 14 November. ....	27
Figure 30. DUT building area sonic estimated turbulence strength for 15 November. ....	28
Figure 31. The 800-m target area sonic estimated turbulence strength for 15 November. ....	28
Figure 32. The 1800-m target area sonic estimated turbulence strength for 15 November. ....	29
Figure 33. Tower sonic estimated $C_n^2$ data from 2-m level, 15 November. ....	29
Figure 34. Tower sonic estimated $C_n^2$ data from 4-m level, 15 November. ....	30
Figure 35. Tower sonic estimated $C_n^2$ data from 6-m level, 15 November. ....	30
Figure 36. Tower sonic estimated $C_n^2$ data from 8-m level, 15 November. ....	31
Figure 37. Calculated turbulence $X = D/r_0$ parameter for November 13 Lockheed Scintil- lometer Data Set. ....	32
Figure 38. Calculated turbulence $X = D/r_0$ parameter for November 13 Scintec Scintil- lometer Data Set. ....	33

Figure 39. Calculated turbulence  $X = D/r_0$  parameter for November 14 Lockheed Scintil-  
lometer Data Set. .... 33

Figure 40. Calculated turbulence  $X = D/r_0$  parameter for November 14 Scintec Scintil-  
lometer Data Set. .... 34

Figure 41. Calculated turbulence  $X = D/r_0$  parameter for November 15 Lockheed Scintil-  
lometer Data Set. .... 34

Figure 42. Calculated turbulence  $X = D/r_0$  parameter for November 15 Scintec Scintil-  
lometer Data Set. .... 35

---

## List of Tables

---

Table 1. Geospatial coordinates of various locations. ....	4
Table 2. Lengths of various paths used. ....	5

INTENTIONALLY LEFT BLANK.

---

## 1. Introduction

---

Optical turbulence effects on long-range optical imaging systems are well known and well documented, especially for instances of long-range ground to ground imaging. Effects include short-exposure blur, long-exposure blur, and image distortion created by a combination of angle-of-arrival fluctuations of point sources and anisoplanatic decorrelation of the angle-of-arrival variations of different, angularly separated, points in the object plane. Several image processing techniques have been introduced over the past two decades to address these impacts. Approaches include image averaging, turbulence blur spectrum estimation and inverse filtering (deconvolution), angle-of-arrival motion correction through image edge detection, tracking, and dewarping, often based on sub-image patch analysis.

Based on the availability of such techniques, the Defense Advanced Research Project Agency (DARPA) sponsored the creation of a system that syncretistically adopted or adapted several of these processing approaches into a single modular processing unit. The developer is General Dynamics.

Our involvement began in the spring of 2012 when the DARPA project manager determined that a site on White Sands Missile Range (WSMR), NM, would provide a suitable high-turbulence environment that would challenge the capabilities of the Super-Resolution Vision System (SRVS). The site selected for the testing was the U.S. Army Research Laboratory (ARL) Electro-Optical Vulnerability Assessment Facility (EOVAF), maintained by elements of ARL's Survivability/Lethality Analysis Directorate (SLAD). To provide the measurement support at this range, DARPA contacted the present staff who are assigned to the Battlefield Environment Division (BED) of ARL's Computational and Information Sciences Directorate (CISD). The members of this group had previously supported testing of electro-optical systems at another WSMR site in 2005 that involved staff of the Army's Night Vision and Electro-Optical Sensors Directorate (NVESD). NVESD personnel were also present at the test site to provide colocated confirmatory imagery of the same target scenes as the SRVS during testing.

The ARL EOVAF range is located on the eastern border of WSMR proper, at the foot of the Jarilla mountains in the southeastern portion of the range. The EOVAF range is unique at WSMR in that it features a series of seven target points located at 300, 800, and 1800 m from a Device Under Test (DUT) building (or, simply, the DUT). Each target point has its own background provided by an earthen berm some 20 ft tall. A portion of the EOVAF range is shown in figure 1.



Figure 1. Typical vegetation and earthen berms in distance at EOFAF range.

The 300-m target berm was used as a short-range object identification location whereby a target's general features could be assessed under conditions where the turbulence effects would be minimal. The three 800-m target points, along with the three 1800-m points, would then provide suitably challenging cases, particularly when elevated levels of daytime turbulence are taken into consideration. To characterize turbulence effects at different ranges and under varying turbulence conditions, the SRVS test plan featured varying ranges from observers to objects of interest. Both morning and afternoon lines of sight were specified such that the targets could be seen under similar frontal illumination conditions (west-looking in the morning and east-looking in the afternoon). This choice of different morning and afternoon viewing geometries also allowed for the choice of different ranges to the targets of interest. For example, setting up at the DUT and looking westward, one could observe targets at 300, 800, and 1800 m, and a specially sited location at approximately 2000 m in the desert beyond the main EOFAF range. In the afternoon, one could set up at the 1800-m range and view objects at 950 and 1450 m (looking toward the west sides of the 800- or 300-m berms) as well, or locating at the 800-m range one could view targets at 1000 m (1800-m berm) in the morning or 450 m in the afternoon (looking toward the west side of the 300-m berm). The general geometry of the locations and ranges of various target and observation points during the test is shown in figure 2. Geospatial coordinates of various locations are shown in table 1. Lengths of various paths are shown in table 2.



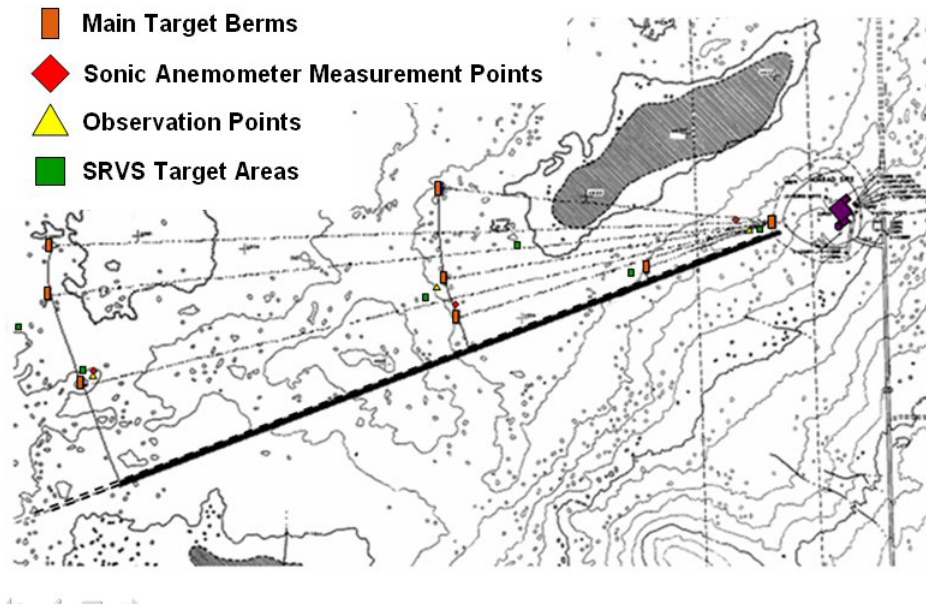


Figure 2. EOVSF range site map for targets, observation points, and sonic anemometer measurement points.

ARL supplied a series of targets for use in estimating turbulence effects on imaging during the test. Two different types of target were supplied. The first was a type of radial bar target typically used by NVESD when testing imaging performance through turbulence. It is shown in figure 3. The second was developed by ARL to show both the impacts of angle-of-arrival of point-like objects in an image field and the ability of a system to resolve high-angular-frequency information at range. This target is shown at figure 4. It was termed the *resolution target* during testing. Four versions of this target were produced. The largest was  $4 \times 4$  ft and placed alongside the  $4 \times 4$  ft radial bar target at 1800 m. A  $2 \times 2$  ft version was placed at 900 m. An  $8 \times 8$  in version was also available for use at 300 m, but was never used, along with a  $1 \times 1$  ft version that was used in combination with other targets sensed at 450-m range. Accompanying the resolution targets were a series of replica military weapon and false alarm targets. Figure 5 shows some of the replica weapons viewed. Figure 6 shows some of the false alarm objects that could be mistaken for weapons.

Table 1. Geospatial coordinates of various locations.

Description of Point	Latitude	Longitude	UTM Easting	UTM Northing	Elevation (m)
Data collection trailer	N32 31.413	W106 08.691	392479	3599047	1235
Sonic anemometer tower	N32 31.413	W106 08.716	392440	3599048	1234
Scint Receiver	N32 31.413	W106 08.706	392455	3599048	1240
Imagers DUT	N32 31.400	W106 08.696	392471	3599023	1240
DUT Sonic anemometer	N32 31.404	W106 08.695	392472	3599031	1239
BLS 450 Receiver	N32 31.402	W106 08.685	392488	3599027	1240
300-m Back of Berm Targets	N32 31.336	W106 08.901	392148	3598909	1234
300-m Top of Berm Targets	N32 31.339	W106 08.890	392166	3598914	1240
300-m Face Targets	N32 31.339	W106 08.899	392152	3598914	1235
300-m Target west side	N32 31.336	W106 08.899	392152	3598909	1242
500-m Target	N32 31.377	W106 09.080	391869	3598987	1232
Scint Trans 800-m	N32 31.278	W106 09.173	391722	3598806	1237
Berm Top 800-m	N32 31.281	W106 09.203	391675	3598812	1241
800-m Rad Target	N32 31.302	W106 09.237	391622	3598851	1234
800-m Optics Table	N32 31.323	W106 09.217	391654	3598890	1237
800-m Ground Target	N32 31.304	W106 09.232	391630	3598855	1234
800-m Sonic	N32 31.296	W106 09.184	391705	3598839	1234
1800-m Targets Day 1	N32 31.204	W106 09.805	390731	3598680	1234
1800-m Optics Table	N32 31.201	W106 09.789	390756	3598674	1229
1800-m Sonic/BLS Xmit	N32 31.206	W106 09.788	390757	3598683	1229
2000-m Targets	N32 31.265	W106 09.912	390564	3598795	1230
DUT by door	N32 31.398	W106 08.675	392503	3599019	1240

Table 2. Lengths of various paths used.

Path Endpoints	Length (m)
DUT to 500-m	603
DUT to 800-m	858
DUT to 1800-m	1773
DUT to 2000-m	1921
800-m optics table to 1800-m	947
1800-m Optics table to 300-m west side	1416
1800-m Optics table to 300-m top	1430
1800-m Optics table to DUT by door	1781
800-m optics table to 300-m west side	498
800-m optics table to 300-m top	513
800-m optics table to DUT imagers	828

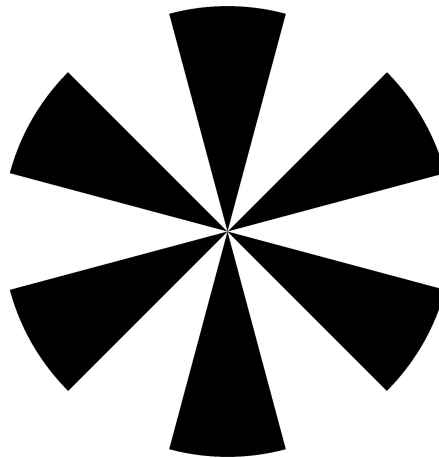


Figure 3. Six-spoke radial bar target image.

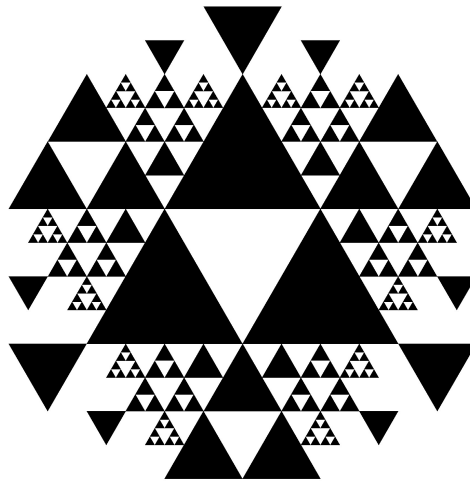


Figure 4. Pseudo-fractal (multi-resolution) target image.



Figure 5. Various replica military weapon targets viewed.



Figure 6. Common objects used as false alarm targets.

---

## 2. Weather During the Test

---

Originally the developmental test was scheduled for May of 2012, but due to delays of various kinds, the schedule slipped until mid-November. This was somewhat unfortunate because turbulence conditions are typically stronger in late spring and summer, with the possible exception of July and August, depending on the timing of local rains that are caused by a monsoonal flow from the Gulf of Mexico during those months. November represents a transitional month, between the commonly dry fall weather (of September and October) that follows the moist and cloudy “monsoon” months of summer, and “winter” months of December through February that can feature a wide range of weather conditions from dry clear days, to windy frontal passages, to winter storms, to rain. November, as a transition month, can feature any of the above combinations, though usually either clear conditions or cloudy conditions with little precipitation. During the actual SRVS testing period the weather was largely cooperative, although a cold front had passed through the area on the Sunday prior to the test, including some rain and cloudcover. However, the Monday morning of the first test day (setup day for the General Dynamics contractors, DARPA Centra Technologies contractors, and NVESD staffers) was clear, dry, and featured relatively mild winds (though it was cool for most of the day).



Diurnal temperatures for the measurement period varied from a low of just below freezing at dawn to high temperatures typically reaching either the high sixties in the afternoon up to perhaps 70 °F on the final day. The weather was generally clear throughout the measurement period on the first two days of testing plus the setup day. The weather changed with the onset of another frontal passage on the afternoon of the final day testing, 15 November. On that day the morning measurements were made under reasonably clear sky conditions. However, in the afternoon, a patch of high cirrus appeared to extend over the range from the southwest, blocking a significant portion of the direct sunlight starting around 1300. At that point turbulence strength dropped in half or more for the remainder of the testing day.

On all test days but the last, the typical trajectory of the turbulence  $C_n^2$  value began with a neutral event around  $10^{-15} \text{ m}^{-2/3}$  at approximately 0720, followed by a rapidly increasing turbulence profile through approximately 1000, at which point the turbulence approximately saturated to its daytime high value of  $1\text{-}2 \times 10^{-13} \text{ m}^{-2/3}$ . This diurnal variation of turbulence was seen by the 1800-m scintillometer. The 800-m scintillometer was located at a slightly lower elevation and thus reported a slightly higher average daytime value. The 1800-m value was found to be approximately equal to the tower-sensed turbulence at 5 m, while the 800-m scintillometer measured its turbulence at a height of approximately 3 m. After about 1300, the  $C_n^2$  value began to diminish toward the evening neutral event minimum.

---

### 3. Atmospheric Instrumentation and Analysis

---

Meteorological instrumentation comprised seven model 81000 RM Young three-dimensional (3-D) sonic anemometers. These were set to sample three wind components plus air temperature at 20 Hz. Anemometers were placed at three target locations used during the week of testing. They were mounted at 1.5-m above ground level (AGL) atop tripods in the yard outside the DUT building, in the 800-m target area, and in the 1800-m target area. One of the downrange tripods is shown in figure 7. In addition, a tower was set up outside the DUT building fence-line with sensors at 2-, 4-, 6-, and 8-m AGL, shown in figure 8. In addition to the seven anemometers, two scintillometers were used to detect path-averaged turbulence strength. One scintillometer sensed turbulence atop a 2-m-tall scaffold on both the emitter and receiver ends of the optical path. The emitter was located at the 800-m target area. The receiver was located just outside the northwest corner of the DUT fence-line. The second scintillometer had the emitter located at the 1800-m target area with its receiver located at the pad just outside the DUT building itself. The 800-m scintillometer path was approximately 2 m lower than the 1800-m scintillometer path. The

800-m scintillometer, moreover, was an older Lockheed scintillometer model (Lockheed transmitter shown in figure 9), while the 1800-m scintillometer was a Scintec model 450 unit. The Scintec unit could measure turbulence at longer range than the Lockheed unit. The latter is range limited to approximately 1 km maximum range prior to saturation.



Figure 7. Downrange tripod with mounted 81000 RM Young sonic anemometer.



Figure 8. Meteorological tower with sonic anemometers at 2, 4, 6, and 8 m.





Figure 9. Lockheed scintillometer transmitter shown just above horizon formed by 800-m berm.

Data collected during evening hours of the test period were restricted to only the sonic data because the Scintec unit relied on a data collection unit and a connection to a laptop computer for data recording. The umbilical connector for this data link had to be disconnected at night to secure the DUT building. Thus only daytime data were available for this unit. Meanwhile, the sonic anemometer data were collected continuously throughout the test period. Raw data has since been quality controlled and provided to test participants.

In the following section we describe the means to estimate the  $C_n^2$  value from the data collected by the sonic anemometers. A subsequent section then describes plots of the various data sets and discusses the intercomparison of results from different instruments.

---

#### 4. Estimation of $C_n^2$ from Sonic Anemometer Data

---

The sonic anemometer instrumentation can be used to provide a point estimate of the turbulence strength based on a few minimal assumptions. This estimate is based on the model of the inertial subrange associated with Kolmogorov's theory that in one dimension the spectral dependence in the subrange varies in strength as  $\kappa^{-5/3}$  power law. Based on this assumed dependence, which relies on the assumption that the atmosphere is stationary in increments (compare with Goodman, 1985), one may evaluate a one-dimensional (1-D) spectrum, derived from a time series of temperature measurements obtained from one of the sonic anemometers over a statistically

significant interval. One may then multiply the high-frequency portion of that spectrum by  $\kappa^{+5/3}$ , where  $\kappa [\text{m}^{-1}]$  is a spatial frequency variable, and attain a function that should be approximately equal to a constant value in the inertial subrange portion of the spectrum. Then, averaging the value of that function over the inertial spectral range should yield a constant that is proportional to the  $C_n^2$  value.

Numerically, we describe the relationship between  $C_n^2$  and temperature fluctuations using a restricted model. We assume, and this is almost true for the measurements made, that humidity fluctuations only contribute a minor perturbation to the calculation. In actuality, humidity effects may contribute up to a 10% variation, but in terms of measurements that vary by orders of magnitude such contributions are effectively “in the noise,” since often turbulence strength can vary by a factor of two over less than a minute. Also, humidity impacts are relatively minor at visible through infrared wavelengths, only becoming truly significant at radio frequencies.

Hence, we can write,

$$C_n^2 = (\partial n / \partial T)^2 C_T^2, \quad (1)$$

where  $n$  is the refractive index function,  $T$  is the absolute temperature in Kelvin, and we write the derivative with respect to temperature as,

$$\frac{\partial n}{\partial T} \approx -78.2 \times 10^{-6} \frac{P}{T^2}, \quad (2)$$

where  $P$  is the atmospheric pressure in millibars. The remaining quantity is  $C_T^2$ , which is the temperature structure parameter.

Both  $C_n^2$  and  $C_T^2$  are related to similar structure functions of the type,

$$D_R(\vec{r}) = \langle [R(\vec{x} + \vec{r}) - R(\vec{x})]^2 \rangle = C_R^2 r^{2/3}, \quad (3)$$

given  $\ell_o \ll r \ll L_o$ , where  $r = |\vec{r}|$  is a scalar separation, and  $\ell_o$  and  $L_o$  are the inner and outer scales of turbulence, respectively. One may think of  $\ell_o$  and  $L_o$  as being the bookends of the inertial subrange. According to the theory of Kolmogorov who initially postulated the concept of the inertial subrange, both temperature and refractive index fluctuations will exhibit structure functions of the type indicated above in the inertial subrange, thus defining  $C_T^2$  and  $C_n^2$  with relation to variables of type  $R$  and its associated  $C_R^2$ .

Related to the structure function for any variable  $R$  is a corresponding 3-D spectrum of  $R$  fluctuations that may be expressed for its inertial range behavior by,

$$\Phi_R(\kappa_3) = \beta C_R^2 \kappa_3^{-11/3}, \quad (4)$$

where  $\kappa_3$  is a 3-D radial frequency variable. That is,  $0 \leq \kappa_3 < \infty$ . The  $\beta$  variable is found as a result of an integration, having the value  $\beta \approx 0.033$ .

However, one never actually measures the 3-D spectrum. The fluctuations measured by the sonic anemometers are a 1-D time sequence. We may define a 1-D spectrum associated with this 3-D spectrum using the integral relation:

$$V_R(\kappa_1) = \int_0^\infty \Phi_R \left( \sqrt{\kappa_1^2 + \kappa_r^2} \right) 2\pi \kappa_r d\kappa_r \approx \frac{6\pi}{5} \beta C_R^2 \kappa_1^{-5/3}, \quad (5)$$

for  $\kappa_1$  in the inertial subrange frequency interval. One can also use a relation due to Tatarskii (equation [1.27] of Tatarskii [1961]) to relate the 1-D spectrum back to its 3-D form:

$$\Phi_R(\kappa) = -\frac{1}{2\pi \kappa} \frac{dV_R(\kappa)}{d\kappa}. \quad (6)$$

The means of connecting this 1-D spectral model to our measurement set is again from Tatarskii: “If in a homogeneous and isotropic field we single out any straight line and consider the field values along only this line, then as a result we obtain a random function of one variable  $x$ , to which we can apply all the results pertaining to stationary random functions.” In particular, our sonic anemometer measurements function as samples of such a straight line (almost) as long as the wind direction is relatively stable for a reasonable period of time. In this case, we may characterize the mean wind speed by the variable  $W$ , and assign temporal frequencies (in Hertz) that we designate by the variable  $f$  obtained by taking a temporal Fourier transform of a series of sonic sample data. The frequency variable  $f$  may then be related to an equivalent spatial frequency variable via the relation,  $\kappa_1 = 2\pi f/W$ .

In turn, we must define the frequency  $f$  in terms of an index variable from the numerical Fourier transform algorithm. Consider a sequence,  $T'_j$ , where  $T'$  is a perturbation temperature and  $j$  is an index variable that ranges from 0 to  $J - 1$ , where for our Fast Fourier Transform (FFT) method  $J = 2^m$ , where  $m$  is an integer. Following standard FFT techniques, we may write the

transformed perturbation temperature as the spectrum,

$$\Theta_l = \frac{1}{J} \sum_{j=0}^{J-1} T'_j Q_{lj}^J, \quad (7)$$

where  $Q_{lj}^J$  is the transform kernel, and a physical frequency  $f$  may be associated with the index  $l$  via the relation  $f = Sl/J$ , where  $S$  is the sample frequency (20 Hz). From this spectrum, the temperature power spectrum can be computed as,

$$P_T(f) = \Theta(+f) \Theta(-f) J/S, \quad (8)$$

such that the dimensions of this power spectrum are  $K^2 s$ . We can use positive and negative frequencies since  $\Theta^*(+f) = \Theta(-f)$  as a consequence of  $T'_j$  being a series of real valued quantities (where the asterix represents complex conjugation).

This power spectrum, based on temporal frequency  $f$ , however, must be transformed into a power spectrum based on spatial frequency  $\kappa_1$ . To do so, we use the transformation (compare with Kaimal et al., 1972)

$$f P_T(f) = \kappa_1 V_T(\kappa_1). \quad (9)$$

That is,

$$V_T(\kappa_1) = f P_T(f)/\kappa_1 = P_T(f) \frac{W}{2\pi}, \quad (10)$$

finally, solving the equivalent of equation 5 where the governing parameter is temperature (i.e., for  $C_T^2$ ), we obtain the relation,

$$C_T^2 = \frac{5}{6\pi\beta} \left( \frac{2\pi}{W} \right)^{2/3} \langle f^{5/3} P_T(f) \rangle_K, \quad (11)$$

where the angle brackets denote an averaging over the Kolmogorov portion (the inertial subrange portion) of the sensed spectrum. We see that this result checks out dimensionally, since  $C_T^2$  must have dimensions of  $K^2 m^{-2/3}$ .

## 5. Data Plots

In this section the various data sets collected are plotted. We first consider the data from the two scintillometers. Figures 10 and 11 show data collected from November 13 for the Lockheed scintillometer measuring  $C_n^2$  along the 800-m path between the DUT and the 800-m target area

and for the Scintec BLS 450 measuring  $C_n^2$  along the 1800-m path between the DUT and the 1800-m target area, respectively.

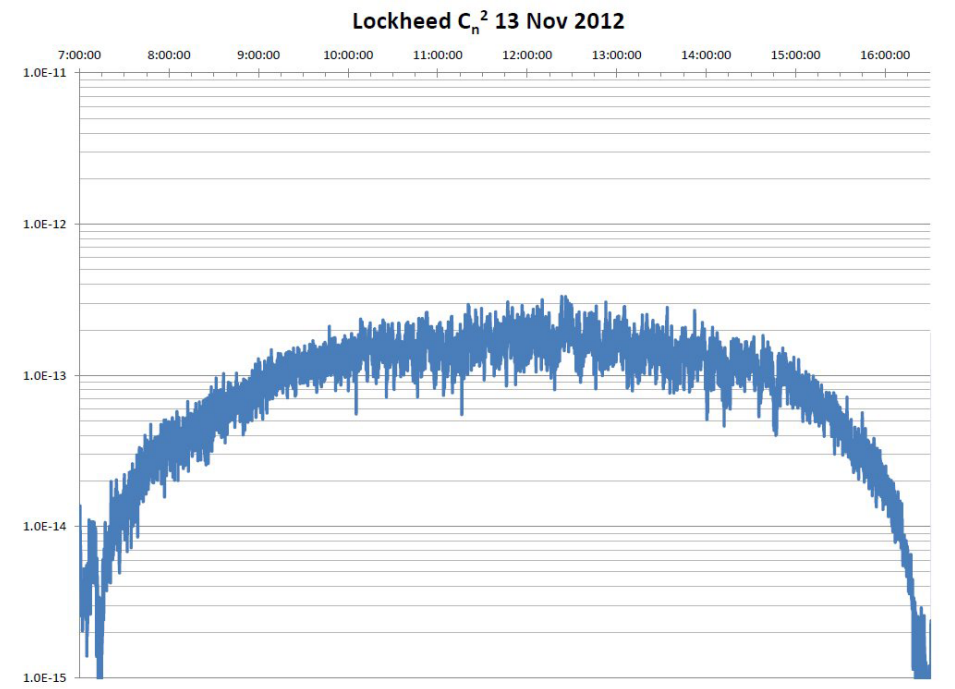


Figure 10. The 800-m Lockheed Scintillometer Data collected on 13 November.

For data collected on this date, two features are of interest. The first is very smooth mean values of  $C_n^2$  in both plots (after removing the high-frequency noise). The second is that the BLS 450 graph begins midday. The BLS instrument had been used the previous week on a different experiment and only became available on the morning of November 13.

Figures 12 and 13 show similar graphs of  $C_n^2$  for data collected on the November 14.

Data collected on November 14, as reported in figures 12 and 13, illustrate the continued good weather for the test period where the turbulence strength tracks as a function of time of day indicate very smooth variations (indicating zero cloud cover and minimal variations due to winds). The track also illustrates the late breaking (with a neutral event around 8:00 a.m. local time) of what appears to have been a very strong surface-based inversion layer. This period would have provided exceptional daytime seeing conditions for viewing targets under extremely low turbulence conditions.

Figures 14 and 15 show similar graphs of  $C_n^2$  for data collected on November 15.

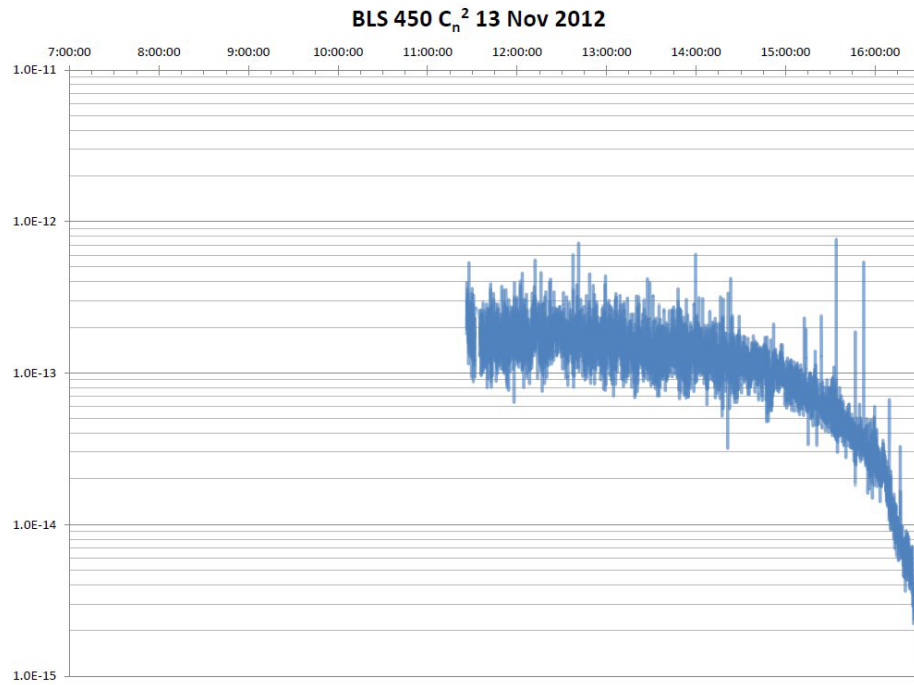


Figure 11. The 1800-m Scintec BLS 450 Scintillometer Data collected on 13 November.

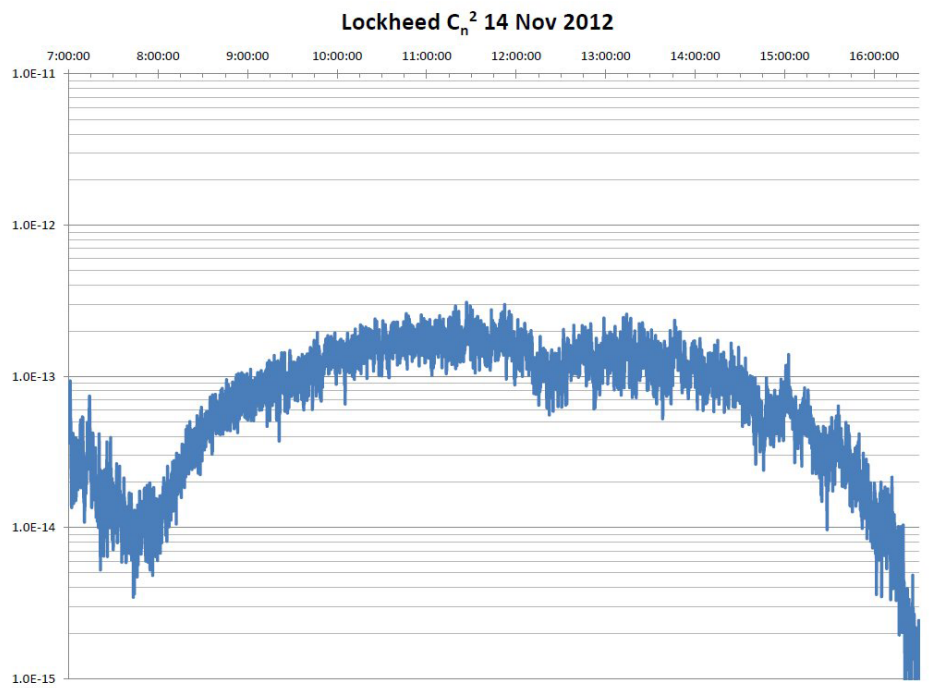


Figure 12. The 800-m Lockheed Scintillometer Data collected on 14 November.

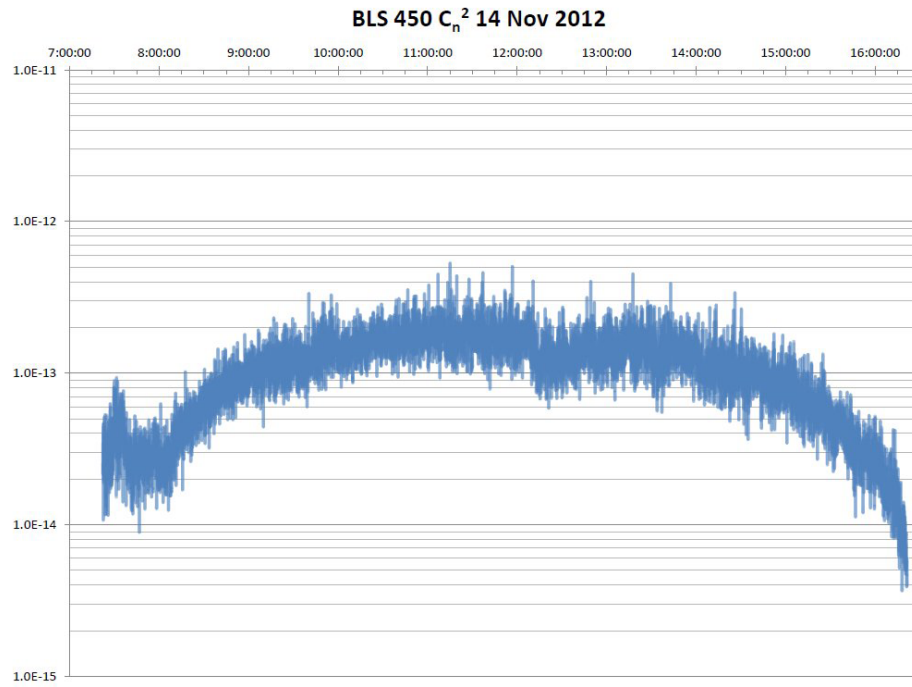


Figure 13. The 1800-m Scintec BLS 450 Scintillometer Data collected on 14 November.

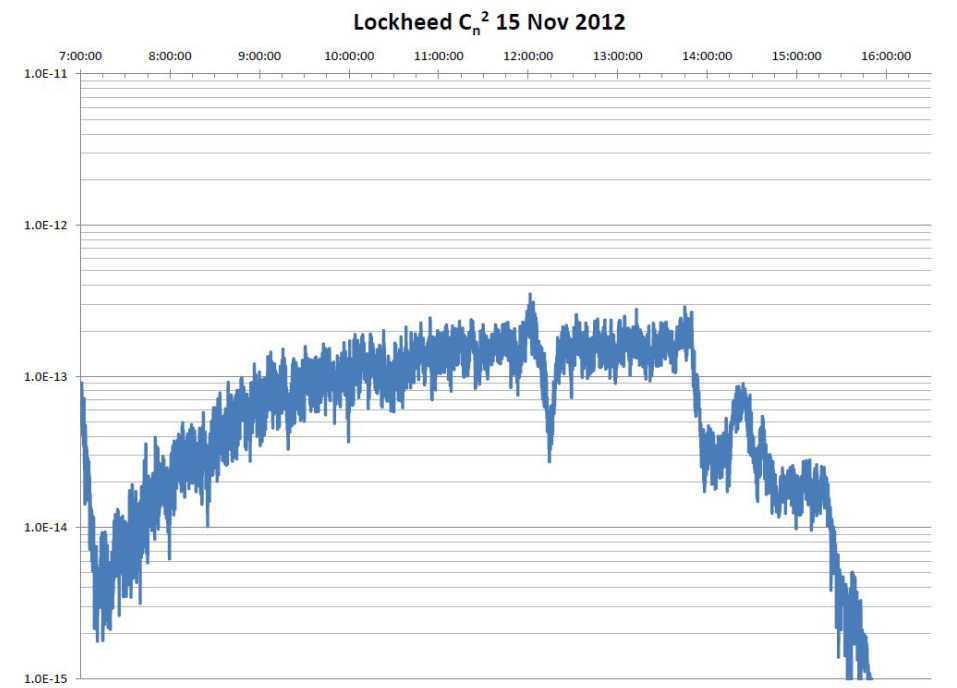


Figure 14. The 800-m Lockheed Scintillometer Data collected on 15 November.

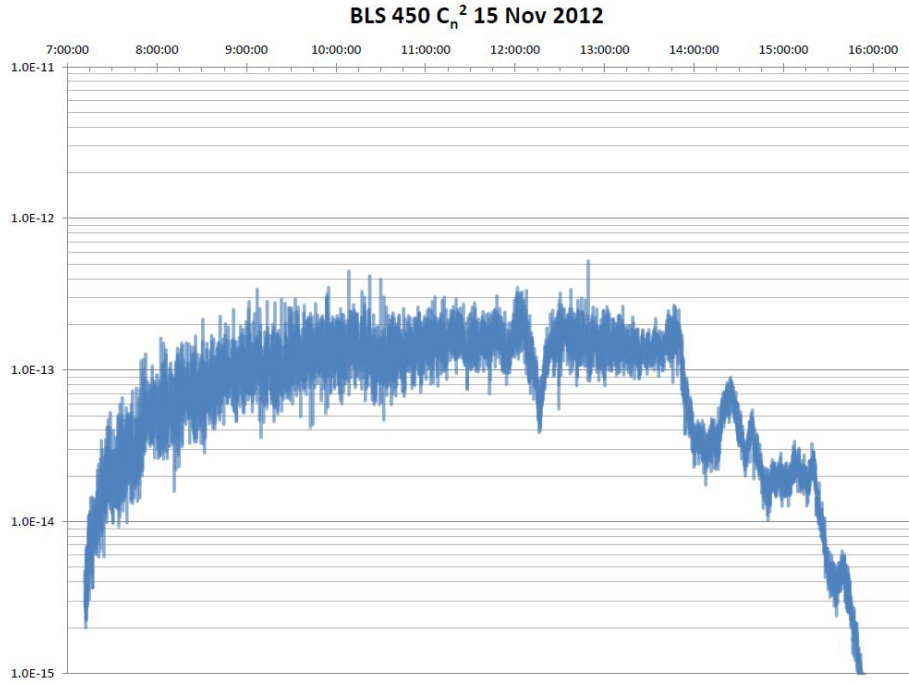


Figure 15. The 1800-m Scintec BLS 450 Scintillometer Data collected on 15 November.

Data collected on November 15 in figures 14 and 15 now detail the impact of encroaching cirrus cloud cover that moved into the area from the southwest that afternoon. Typical of weather patterns in November, cirrus clouds are easily formed at upper altitudes, particularly by jet contrails. These can then grow depending on the specific altitude at which they were formed and details of the available moisture at that level. This cloud cover presence eventually led to an early neutral event occurring around 4:00 p.m. local time.

The other consistent feature of the scintillometer data sets was that although at first glance the Lockheed scintillometer appeared to be sensing turbulence at a lower overall height than the BLS 450 unit placed at the top of the berm beneath the DUT building site, the BLS sensed  $C_n^2$  values appeared to be consistently higher. Two possible explanations of this situation will need to be resolved based on future testing. The first possibility is geography related. For although the Lockheed unit was at a lower overall elevation, it is known that the terrain drops off in the area between the DUT and the 800-m target areas, making the line of sight correspond to approximately 4-m AGL at the path center. The Scintec scintillometer, on the other hand, appears to be higher above the local terrain at the receiver end of the path, but because it is observing a source at the 1800-m range, its path center is at around the 800–900-m range. And at that range, the terrain rises to close to the optical line of sight. Hence, the 1800-m scintillometer



path may be closer to the surface at the path center (where the path weighting effect of scintillation is strongest) than for the 800-m sensor.

We next consider the  $C_n^2$  estimates derived from the point sensor sonic anemometers placed in the DUT building area, the 800-m target area and the 1800-m target area for data collected on November 13. These data are shown in figures 16–18.

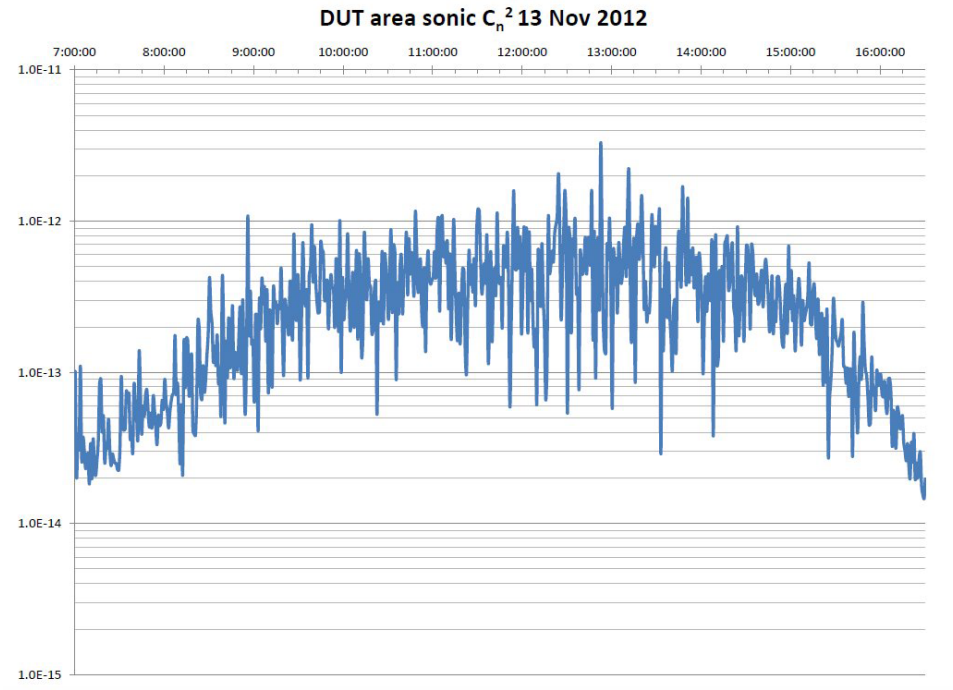


Figure 16. DUT building area sonic estimated turbulence strength for 13 November.

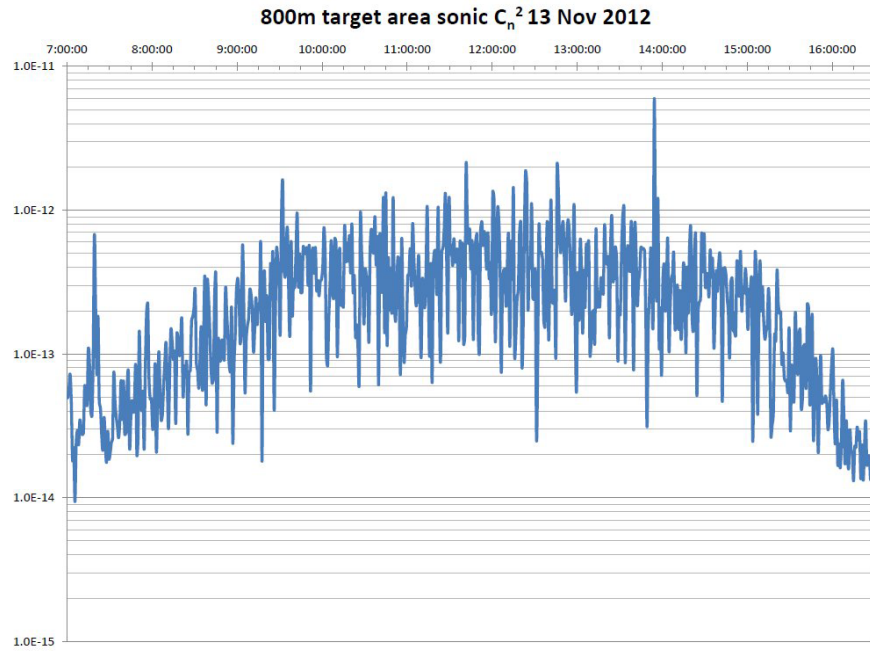


Figure 17. The 800-m target area sonic estimated turbulence strength for 13 November.

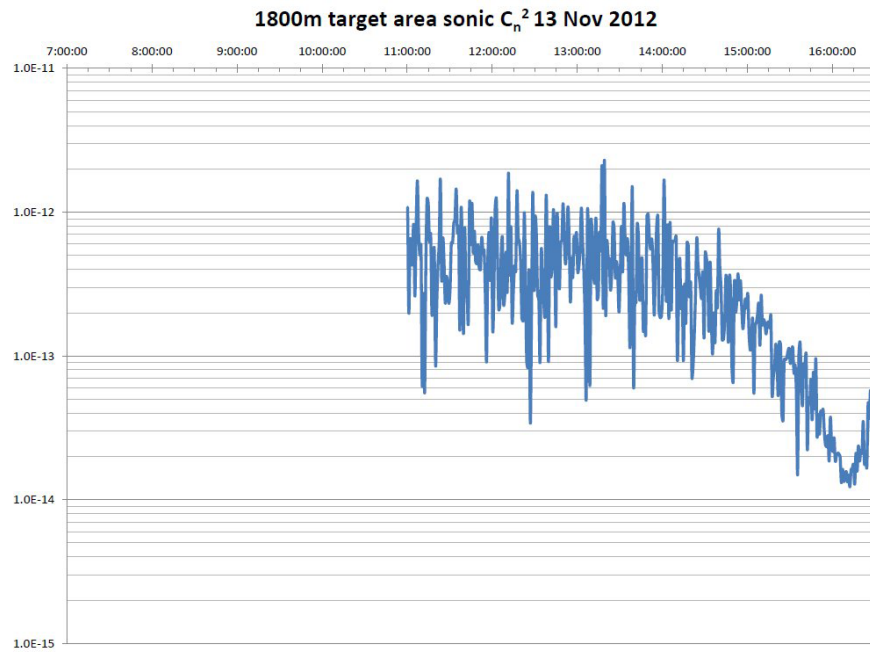


Figure 18. The 1800-m target area sonic estimated turbulence strength for 13 November.

These data may be compared to the data sets collected from the profile tower at 2-, 4-, 6-, and 8-m levels on the same day, as shown in figures 19–22.

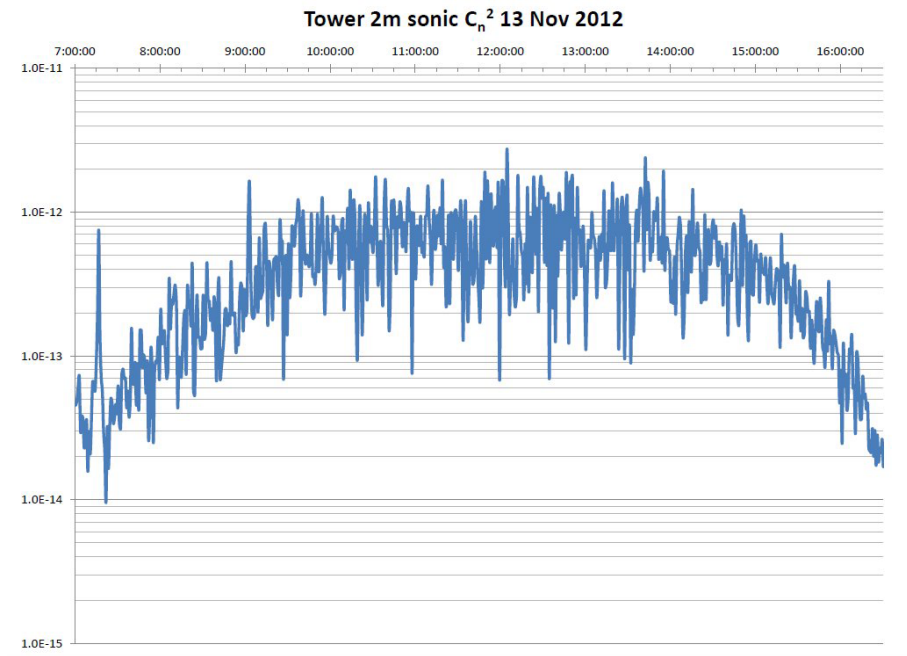


Figure 19. Tower sonic estimated  $C_n^2$  Data from 2-m level, 13 November.

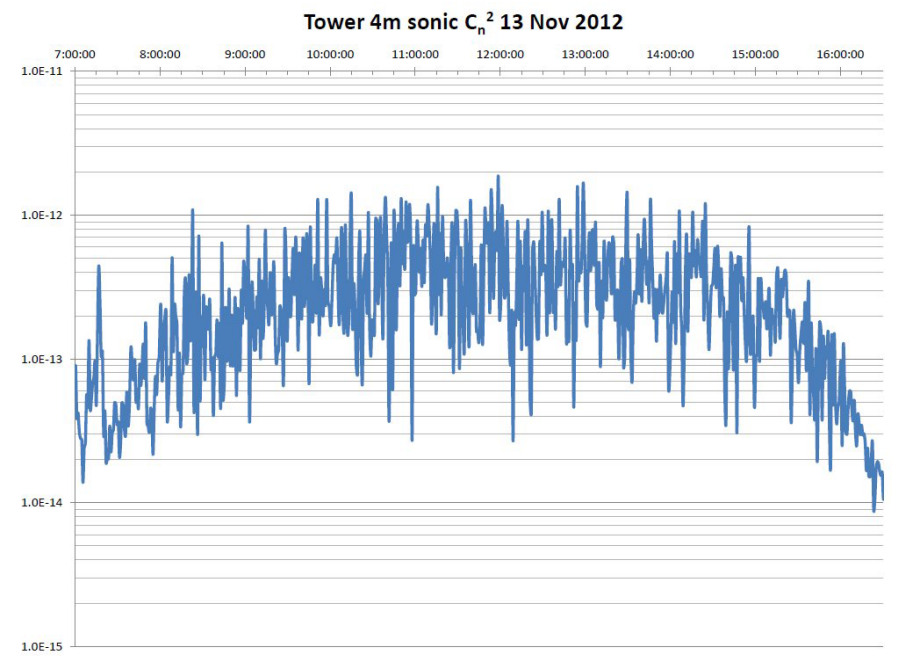


Figure 20. Tower sonic estimated  $C_n^2$  Data from 4-m level, 13 November.

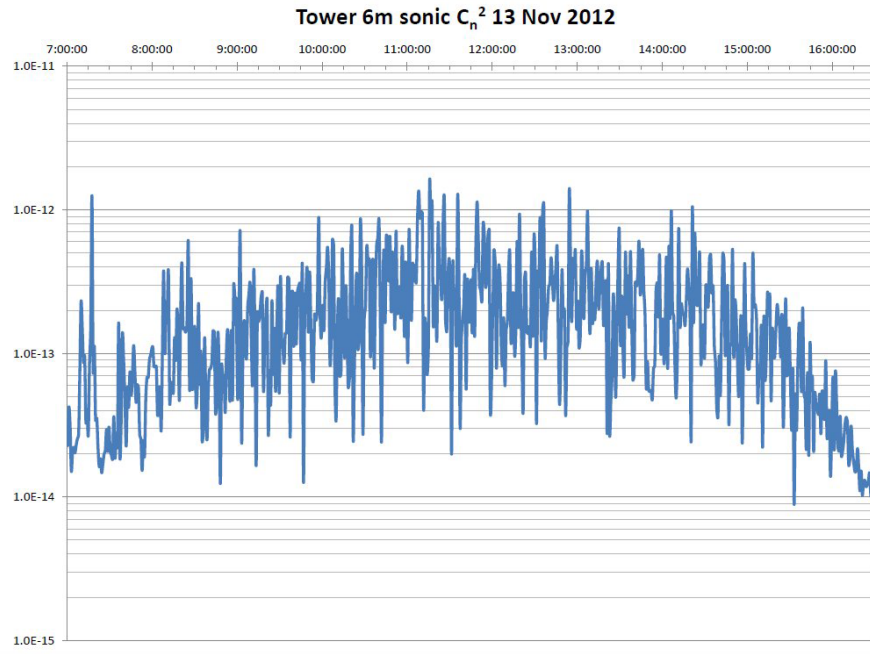


Figure 21. Tower sonic estimated  $C_n^2$  Data from 6-m level, 13 November.

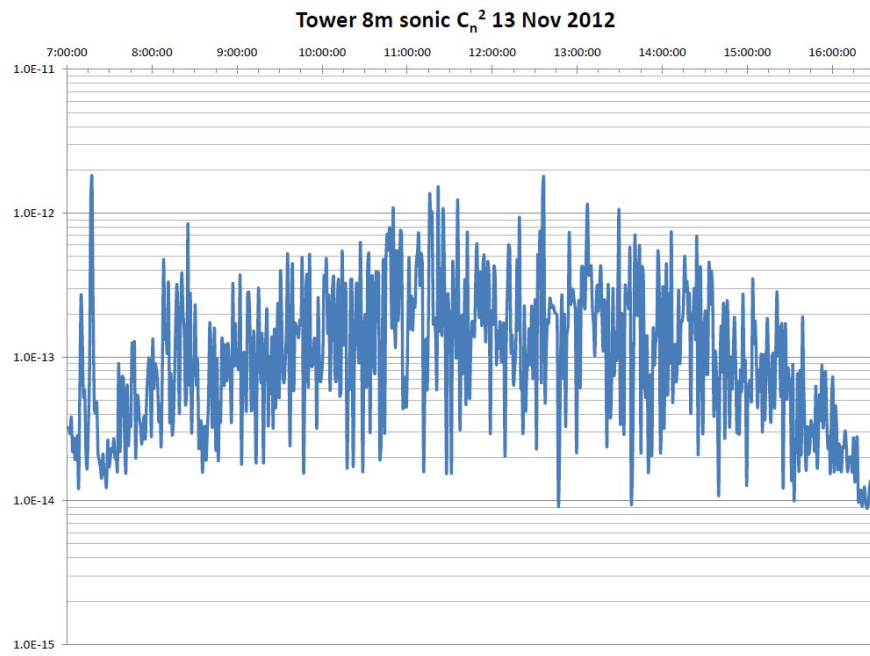


Figure 22. Tower sonic estimated  $C_n^2$  Data from 8-m level, 13 November.

The sonic derived  $C_n^2$  data from November 13 are consistent with data sets collected by the 800- and 1800-m scintillometers. All sets reveal an example of typical clear weather conditions for the site for this time of year.

However, it is interesting to note that the level of  $C_n^2$  varies somewhat depending on the measurement site and height. Most obvious are the variations in  $C_n^2$  with height on the measurement tower. Comparing these tower measurements with the data collected at the point sensors, for example, the  $C_n^2$  values at noon on November 13 are (approximately)  $5 \times 10^{-13}$  at all three of the point sensors, but roughly  $8 \times 10^{-13}$  at the 2-m level on the meteorological tower. This decreases to  $6 \times 10^{-13}$  at the 4-m level, and  $3 \times 10^{-13}$  at the 6-m level. Hence, one may assume that the point sensors at the berms and the DUT represent higher-level measurements than the tower data. The difference may be explained to some degree by the fact that the target berms and the DUT represent elevated locations in the desert, while the meteorological tower was more or less embedded in the desert mound structure of the mesquite vegetation. The 1.5-m levels on the propagation points thus appear to represent heights of approximately 5 m above the actual terrain ground level.

On the other hand, comparison between the scales of turbulence, even using the 6-m level appears to show a turbulence level roughly twice that of the scintillometer data. Here, the issue may be with the means of turbulence calculation used to estimate the  $C_n^2$  using the sonic data. There may, indeed, be a factor of 2 difference present in the calculation because of the difference of a single sided Fourier transform versus a two-sided transform.

Similar results are shown for data collected on November 14. Figures 23–25 are again plots of the point sensors for November 14.

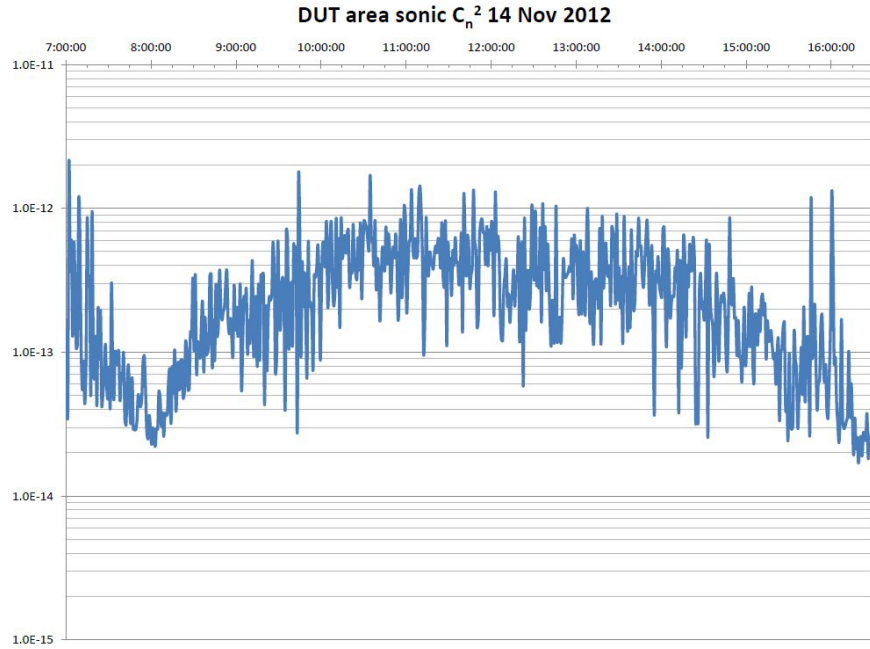


Figure 23. DUT building area sonic estimated turbulence strength for 14 November.

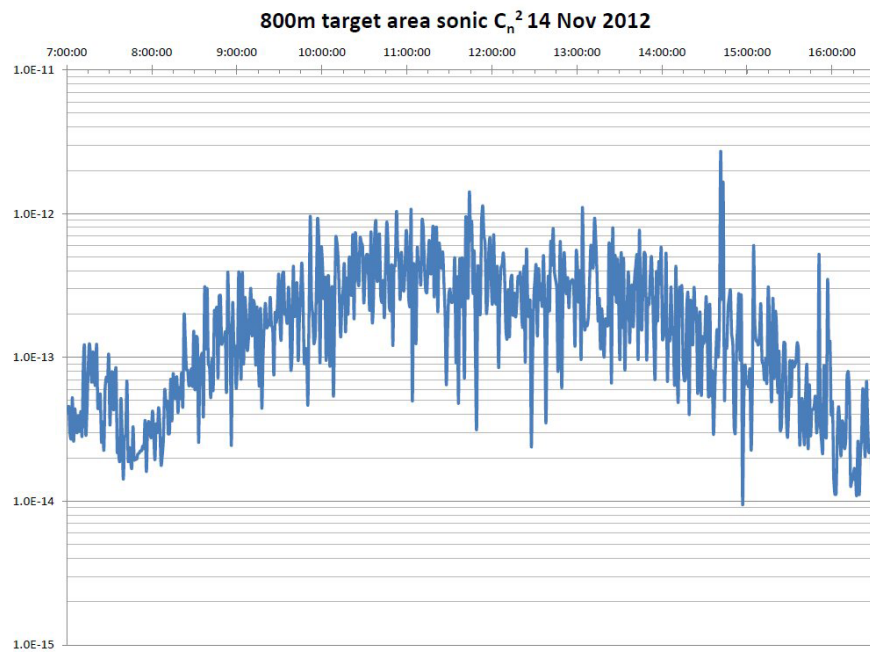


Figure 24. The 800-m target area sonic estimated turbulence strength for 14 November.

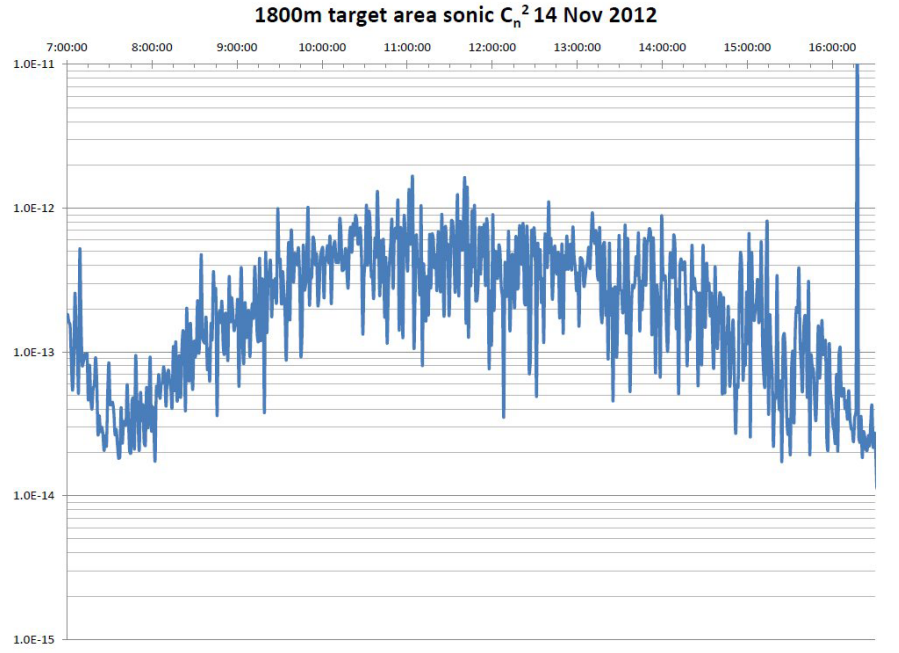


Figure 25. The 1800-m target area sonic estimated turbulence strength for 14 November.

Figures 26–29 then provide the data sets collected from the meteorological tower.

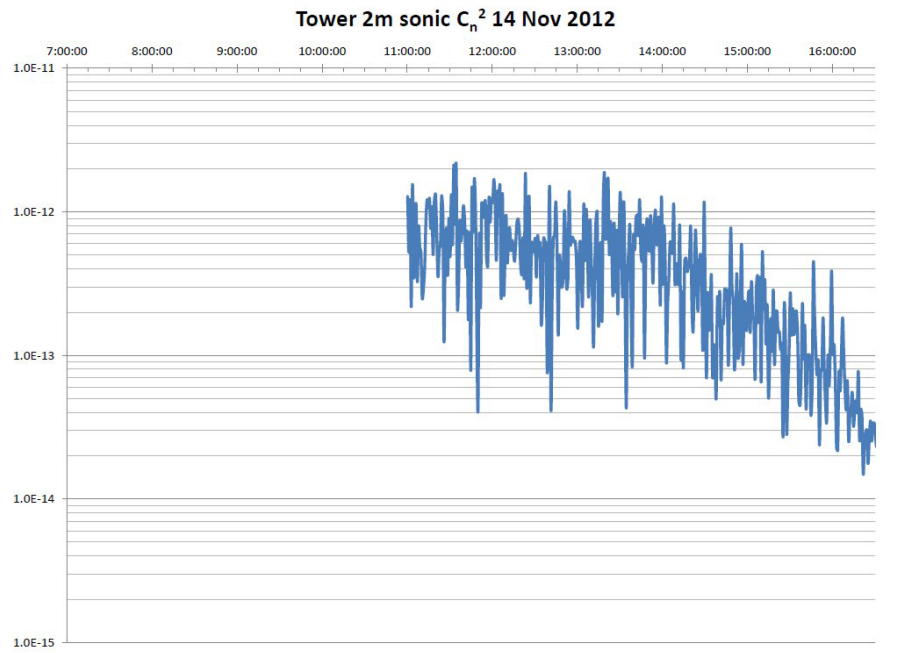


Figure 26. Tower sonic estimated  $C_n^2$  data from 2-m level, 14 November.

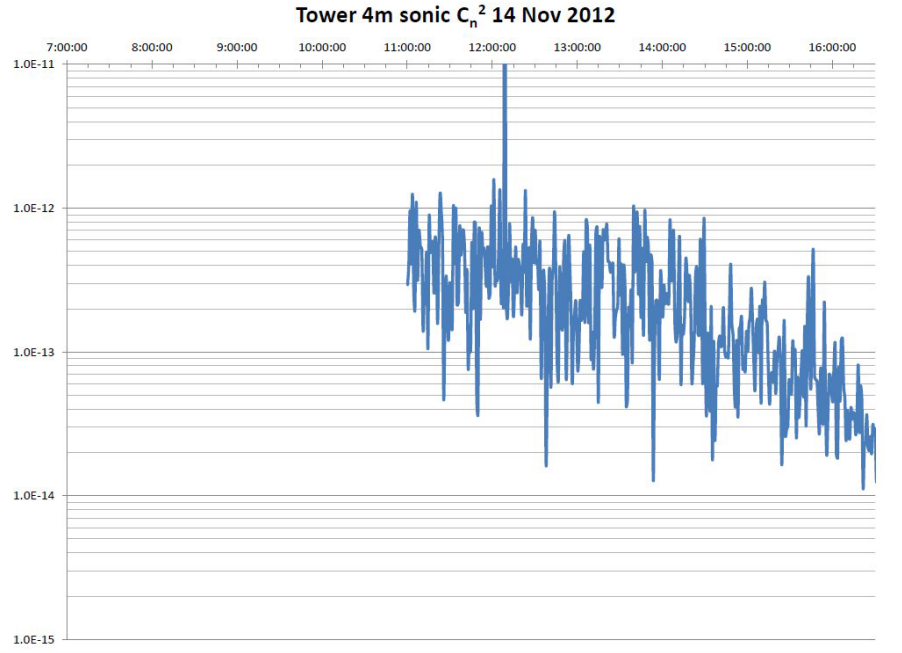


Figure 27. Tower sonic estimated  $C_n^2$  Data from 4-m level, 14 November.

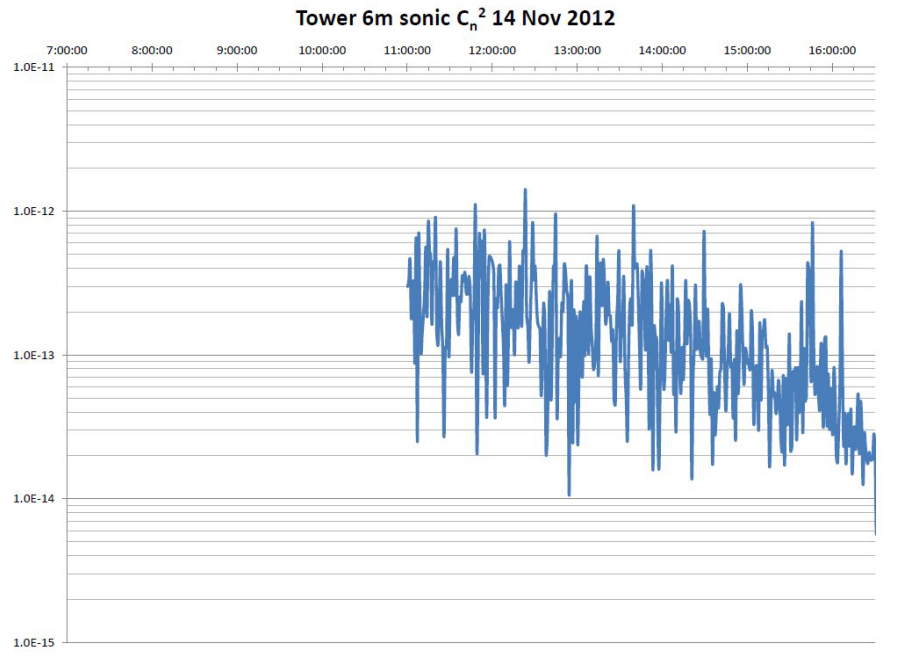


Figure 28. Tower sonic estimated  $C_n^2$  Data from 6-m level, 14 November.

Weather conditions for November 14 were similar to those of November 13. Clear conditions again prevailed.



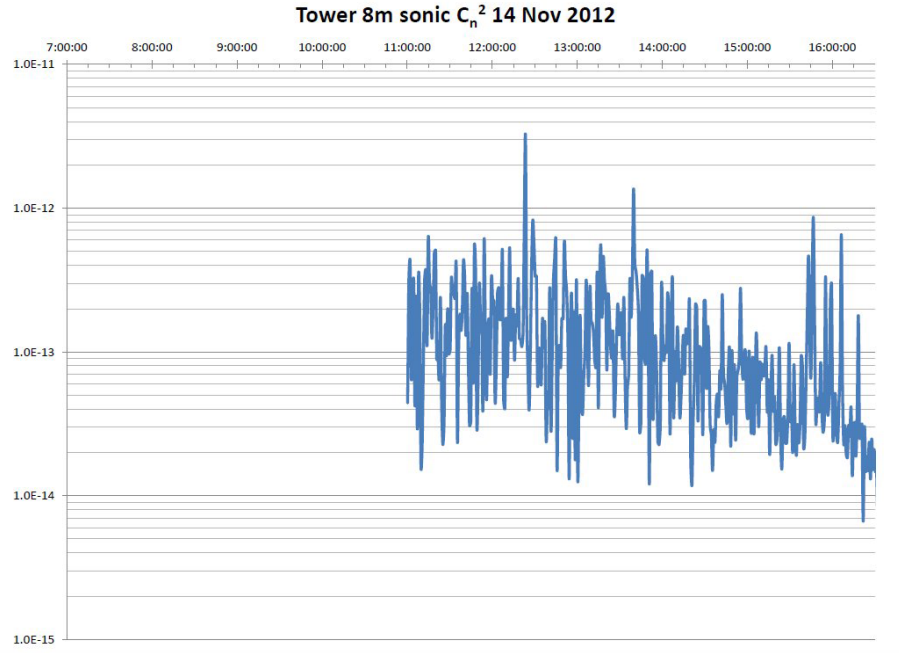


Figure 29. Tower sonic estimated  $C_n^2$  Data from 8-m level, 14 November.

We should also mention at this point that there are clear differences between the amount of variability in  $C_n^2$  values sensed by the sonic sensors compared to the scintillometers. These differences can be explained due to the point nature of the sonic data versus the line integrating properties of the scintillometers. Path averaging experienced by the scintillometer data can of course be simulated somewhat through longer time averaging of the sonic data sets, but this makes comparison between the two sets problematic because we are comparing spatial and temporal overlaps for a diurnally varying parameter.

Lastly, we plot data sets collected on November 15. Figures 30–32 provide the point sensor data plots, and figures 33–36 are plots of data collected from the meteorological tower.

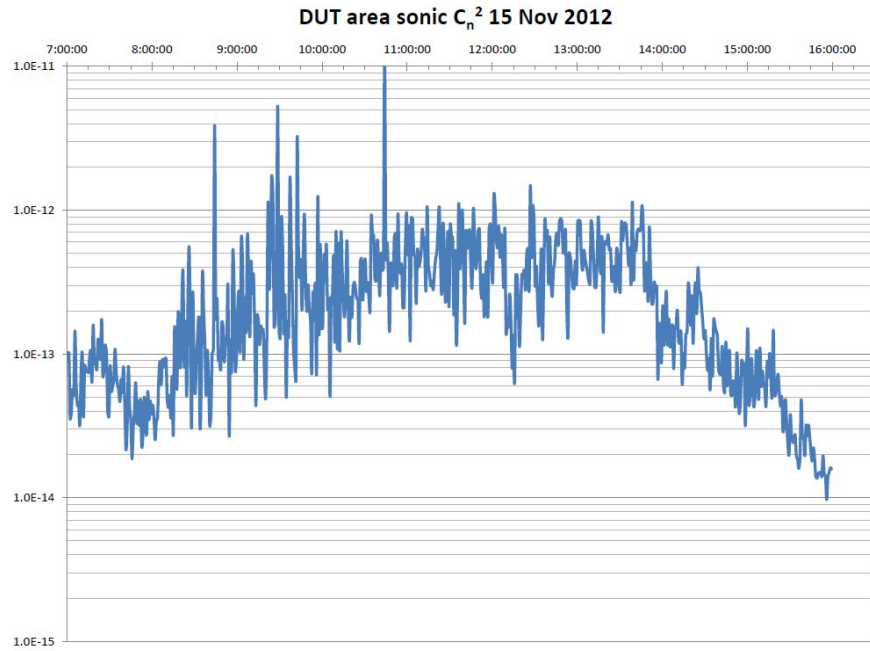


Figure 30. DUT building area sonic estimated turbulence strength for 15 November.

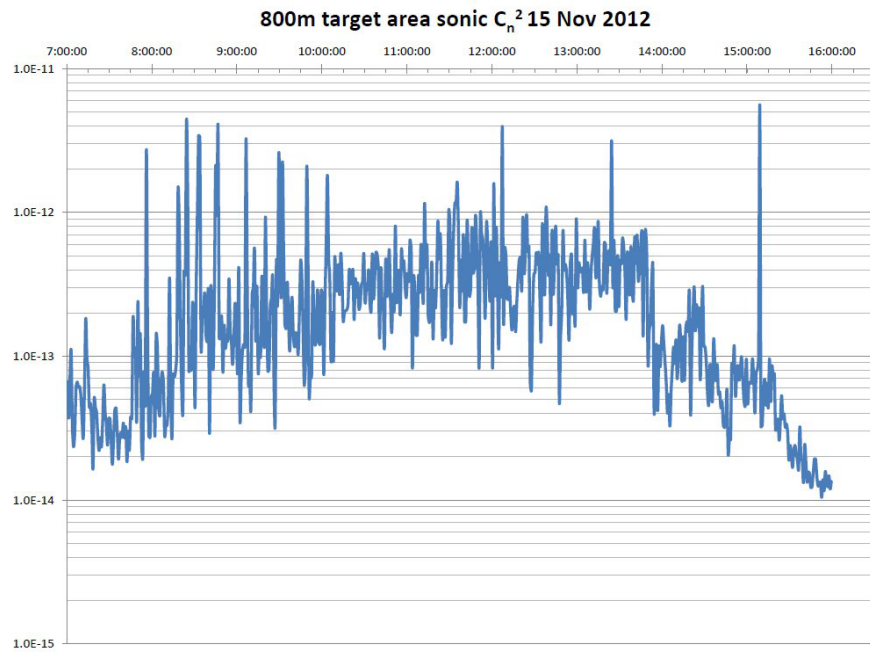


Figure 31. The 800-m target area sonic estimated turbulence strength for 15 November.

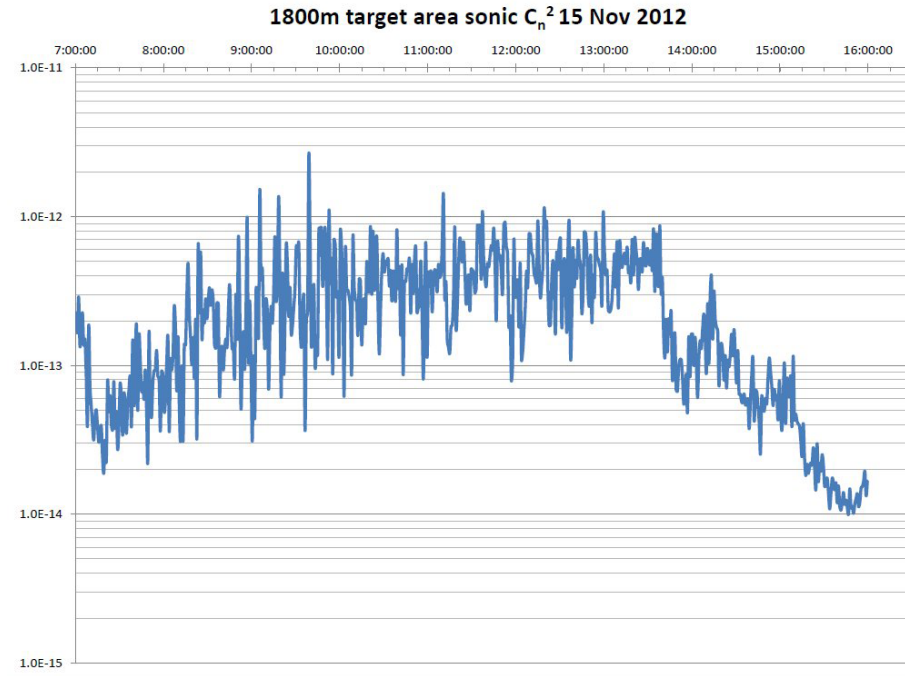


Figure 32. The 1800-m target area sonic estimated turbulence strength for 15 November.

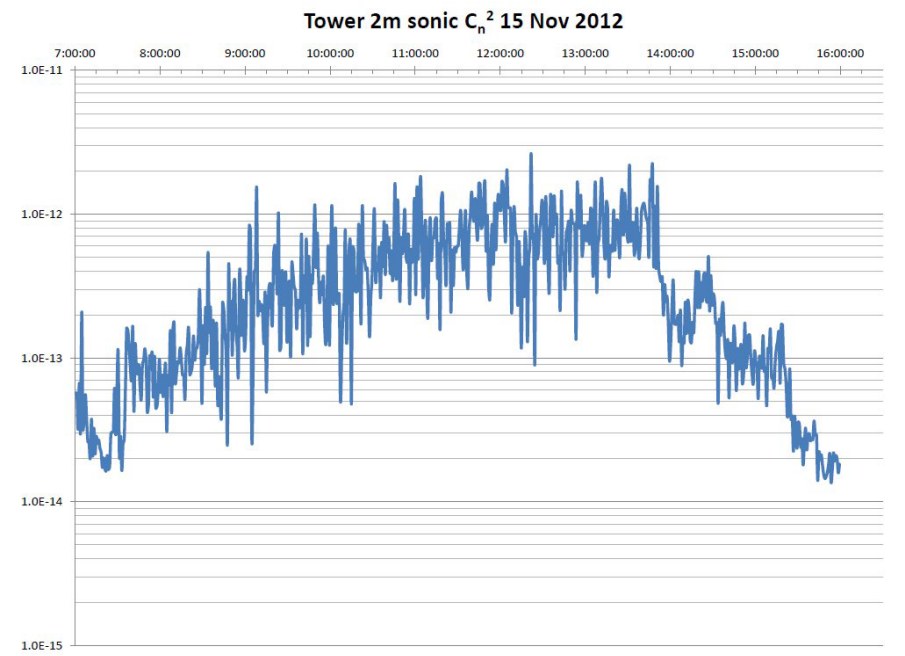


Figure 33. Tower sonic estimated  $C_n^2$  data from 2-m level, 15 November.

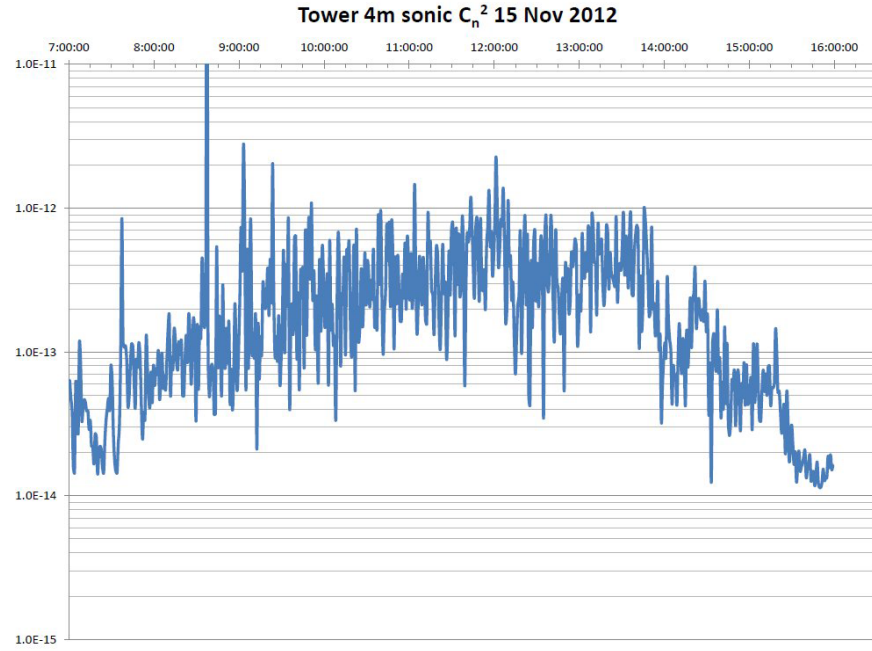


Figure 34. Tower sonic estimated  $C_n^2$  data from 4-m level, 15 November.

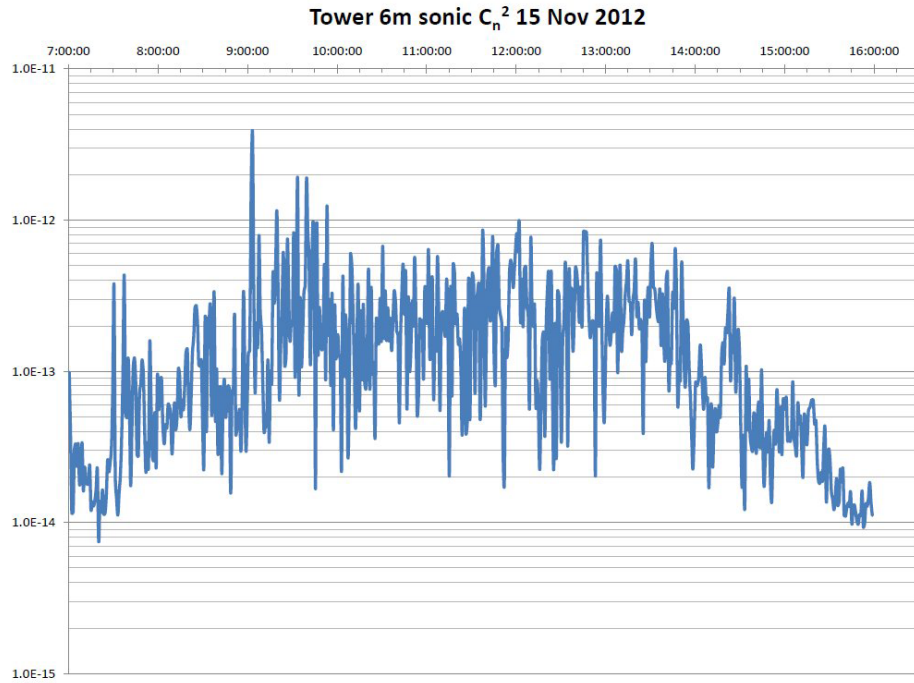


Figure 35. Tower sonic estimated  $C_n^2$  data from 6-m level, 15 November.

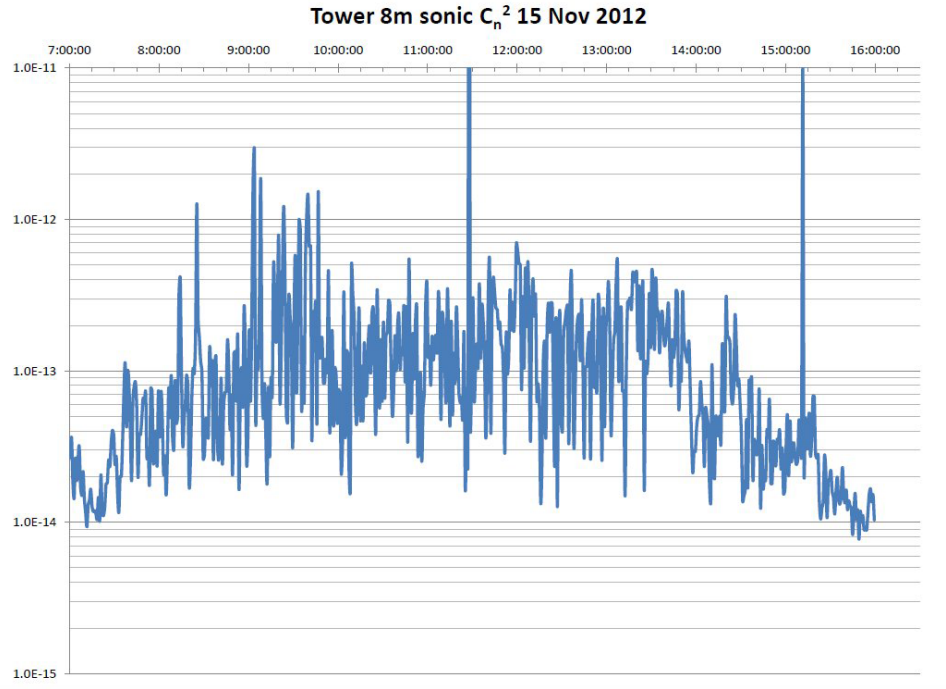


Figure 36. Tower sonic estimated  $C_n^2$  data from 8-m level, 15 November.

Several features of these data sets stand out when comparison is made between data sets collected at different tower levels. The level of turbulence seen is always a diminishing function of height. Perhaps longer averaging periods and plotting of multiple height levels of data on the same plot would have brought this feature out more clearly, which would be useful in a followup paper.

In addition, clearly the variance of turbulence sensed at the upper levels of the tower is significantly higher than the variance of data collected at lower levels. This feature is consistent for all days of the trials. Perhaps the reason behind this is that at the upper levels the outer scale is larger so there are fewer independent samples taken over the course of the 1 min averaging used in the calculation technique. Longer time averaging would tend to wash out this effect, yet keeping these data in this noisy form may be useful in diagnosing variances in turbulence seen in imagery.

We should also point out that the data dropout seen in the data on the morning of November 14 was due to an intermediate data transfer unit that reset itself twice during the same morning. After the second reset it was not caught until the lunch break.

---

## 6. Derived Results

---

In this short section we illustrate something of the significance of the turbulence strength data collected by plotting a computed ratio of the system under test's aperture diameter,  $D = 60$  mm, to the computed coherence diameters based on the scintillometer data collected over the 800- and 1800-m paths. For each data set we selected a wavelength of  $\lambda = 0.55 \mu\text{m}$ , and used the path length associated with the accompanying data. These plots shown in figures 37–42 illustrate the general turbulence strength during the testing period through the dimensionless  $X = D/r_0$  ratio.

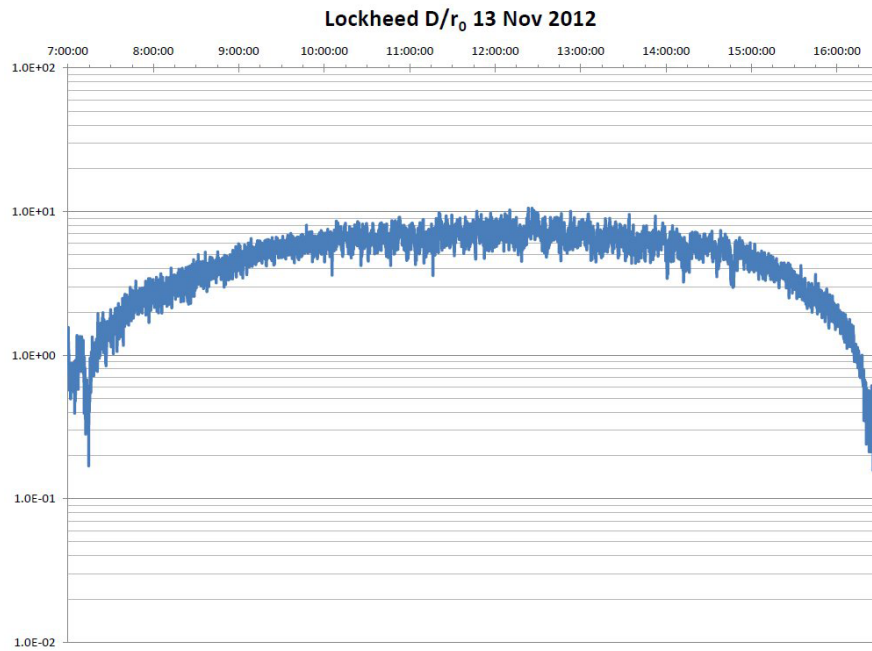


Figure 37. Calculated turbulence  $X = D/r_0$  parameter for November 13 Lockheed Scintillometer Data Set.

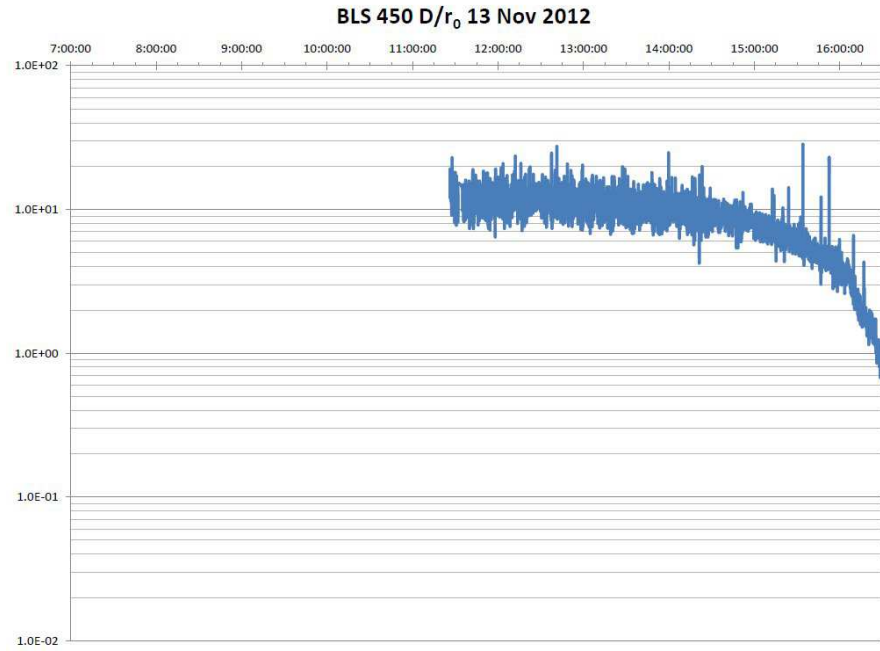


Figure 38. Calculated turbulence  $X = D/r_0$  parameter for November 13 Scintec Scintillometer Data Set.

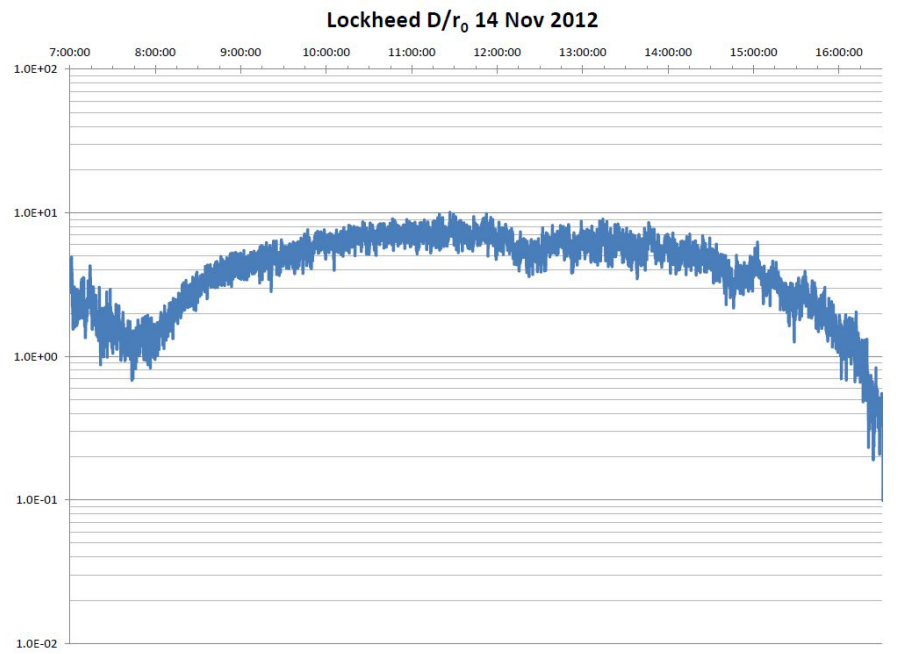


Figure 39. Calculated turbulence  $X = D/r_0$  parameter for November 14 Lockheed Scintillometer Data Set.

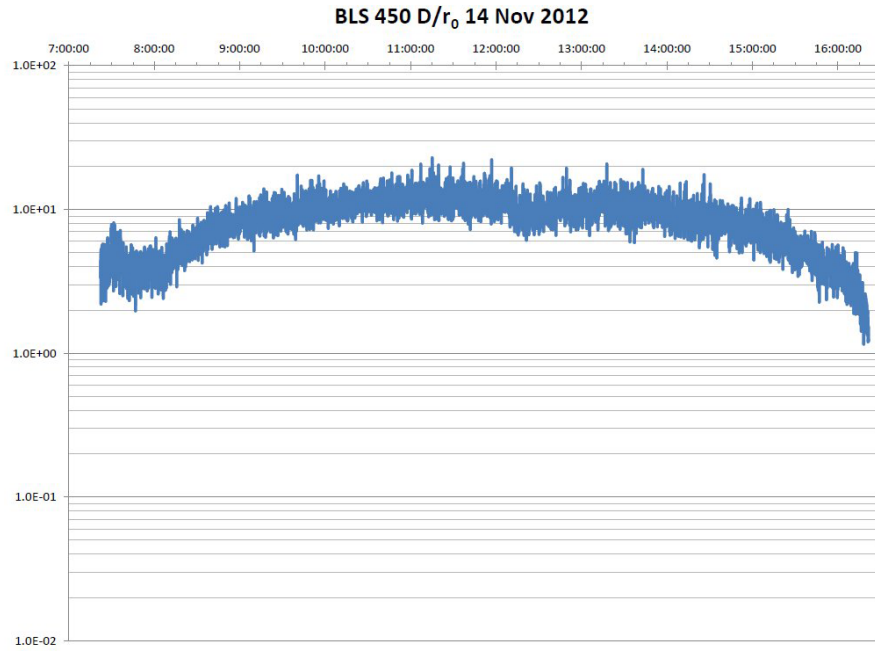


Figure 40. Calculated turbulence  $X = D/r_0$  parameter for November 14 Scintec Scintillometer Data Set.

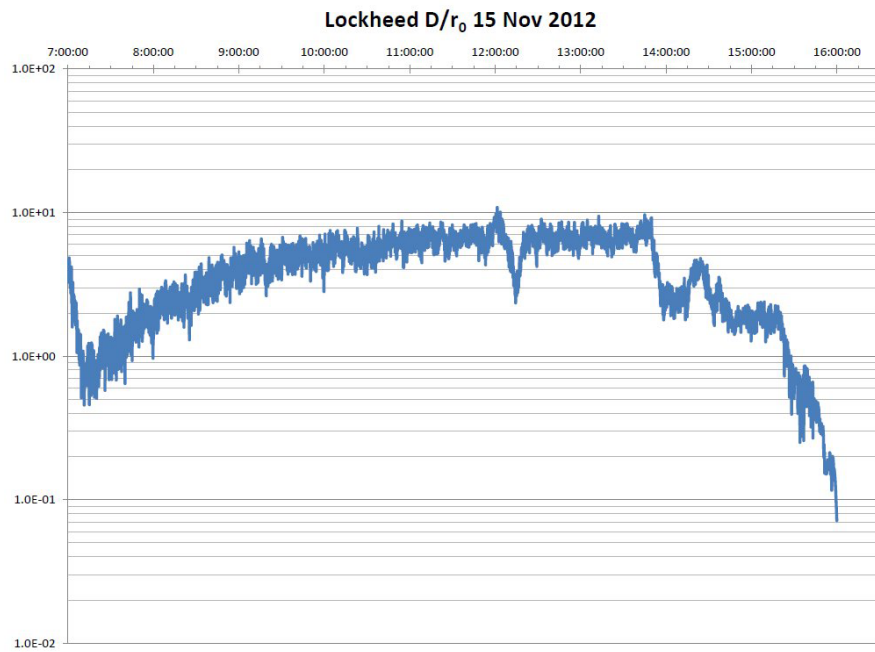


Figure 41. Calculated turbulence  $X = D/r_0$  parameter for November 15 Lockheed Scintillometer Data Set.



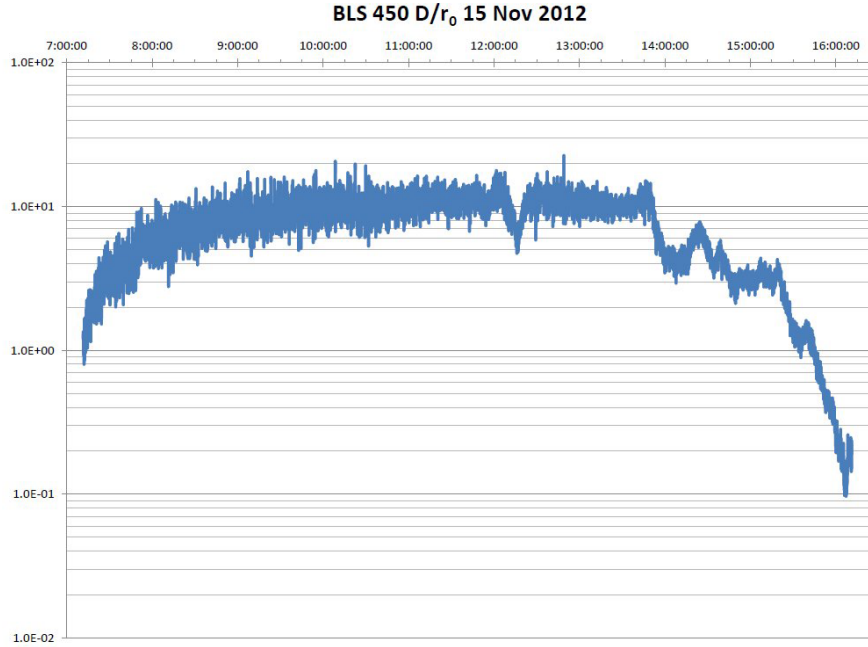


Figure 42. Calculated turbulence  $X = D/r_0$  parameter for November 15 Scintec Scintillometer Data Set.

Six data sets are plotted corresponding to the original scintillometer data plots shown in figures 10–15. For each Lockheed data set a  $X = D/r_0$  plot is given using a range setting of  $L = 800$  m. For each Scintec data set a similar plot is produced using a range of  $L = 1800$  m.

At the 800-m range the  $X$  parameter increased from approximately 2 to 7 between 0730 and 1000 on November 13 and 14. On November 15 the increase was more modest, from 1.5 to 5.5 over the same time interval. At the 1800-m range the same ratio, but computed using the 1800-m range, produced results seldom below 3 during the daytime and often exceeding 10, particularly between 10 a.m. and 2 p.m.

---

## 7. Conclusions

---

The SRVS test provided an opportunity for testing the performance of the system under light to heavy turbulence conditions. Path integrated turbulence strength varied during the testing period from near diffraction limited near the neutral events to  $X/D/r_0$  ratios of 6–8 near midday at the longer ranges. These conditions will be useful to the system to assess turbulence impacts and means of mitigating turbulence in both the system in its present configuration and in assessing means of improving results given available short-range imagery and baseline collection of non-corrected imagery.

---

## 8. References

---

Goodman, J. W. *Statistical Optics*, J. Wiley & Sons, New York, NY, 1985.

Kaimal, J. C.; Wyngaard, J. C.; Izumi, Y.; Côté, O. R. Spectral Characteristics of Surface-Layer Turbulence. *Quarterly Journal of the Royal Meteorological Society* **1972**, 98, 563–589.

Tatarskii, V. I. *Wave Propagation in a Turbulent Medium*, McGraw–Hill Book Company, Inc., New York, NY, 1961.

---

## List of Symbols, Abbreviations, and Acronyms

---

1-D	one-dimensional
3-D	three-dimensional
AGL	above ground level
ARL	U.S. Army Research Laboratory
BED	Battlefield Environment Division
CISD	Computational and Information Sciences Directorate
DARPA	Defense Advanced Research Project Agency
DUT	Device Under Test
EOVAF	Electro-Optical Vulnerability Assessment Facility
FFT	Fast Fourier Transform
NVESD	Night Vision and Electro-Optical Sensors Directorate
SLAD	Survivability/Lethality Analysis Directorate
SRVS	Super-Resolution Vision System
WSMR	White Sands Missile Range

<u>NO. OF COPIES</u>	<u>ORGANIZATION</u>
1 (PDF)	DEFENSE TECHNICAL INFORMATION CTR DTIC OCA
1 (PDF)	DIRECTOR US ARMY RESEARCH LAB RDRL CIO LL
1 (PDF)	GOVT PRINTG OFC A MALHOTRA
1 (PDF)	DIRECTOR US ARMY RESEARCH LAB RDRL CIE D D'ARCY S M

INTENTIONALLY LEFT BLANK.